

Quantum Computing in Corrosion Modeling: Bridging Research and Industry

Juan Manuel Aguiar Hualde¹, Marek Kowalik¹, Lian Remme¹,
Franziska Elisabeth Wolff¹, Julian van Velzen¹, Rene Böttcher²,
Christian Weimer², Jasper Krauser², Emanuele Marsili^{3*}

¹Capgemini Quantum Lab.

²Airbus, Central Research & Technology, Willy-Messerschmitt-Straße 1,
Taufkirchen 82024, Germany.

³Airbus, Central Research & Technology, Pegasus House Aerospace Ave,
Bristol BS34 7PA, United Kingdom.

*Corresponding author(s). E-mail(s): emanuele.marsili@airbus.com;
Contributing authors: juan-manuel.aguiar-hualde@capgemini.com;
marek-jozef.kowalik@capgemini.com; lian.remme@capgemini.com;
franziska-elisabeth.wolff@capgemini.com;
julian.van.velzen@capgemini.com; rene.boettcher@airbus.com;
christian.weimer@airbus.com; jasper.krauser@airbus.com;

Abstract

Corrosion presents a major challenge to the longevity and reliability of products across various industries, particularly in the aerospace sector. Corrosion arises from chemical processes occurring on an atomistic scale, which lead to macroscopic degradation. Addressing this issue requires multi-scale modeling approaches, which rely on microscopic parameters that are challenging to measure experimentally or model with conventional quantum chemistry techniques.

In this work, we develop and demonstrate a hybrid quantum-classical workflow tailored for atomistic simulations of corrosion processes, with a specific focus on the initial step of the oxygen reduction reaction – a critical trigger for the corrosion of aluminum alloys widely used in modern aircraft. Using a combination of classical quantum chemistry methods and quantum computing frameworks, we identify reaction geometries characterized by multi-configurational electronic structures that are ideal for exploring with quantum algorithms.

For the first time in this context, we explore both noisy intermediate-scale quantum and fault-tolerant quantum algorithms for these multi-configurational

system, integrating them within a workflow designed to bridge atomistic simulations with macroscopic modeling approaches, such as finite element methods. Furthermore, we conduct a detailed quantum resource estimation to assess when and how quantum computers may play a meaningful role in tackling these problems.

Our results demonstrate that significant advancements in quantum hardware but also in algorithms and error correction techniques are needed to make quantum computation practically viable for this class of problems. Nevertheless, this work establishes a critical foundation for applying quantum computation to corrosion modeling and highlights its potential to address complex, business-relevant challenges in materials science.

Keywords: Corrosion modeling, Oxygen Reduction Reaction, Quantum Chemistry, Quantum Computing, Variational Quantum Eigensolver, Quantum Phase Estimation, Quantum Resource Estimation

1 Introduction

Corrosion is the degradation of materials, particularly metals, due to chemical or electrochemical reactions with their environment, representing a significant challenge across industries, particularly aerospace, where it affects operational efficiency, vehicle lifespan, and maintenance planning. In this sector, a large variety of aluminum alloys (AA) are utilized, *e.g.*, 2xxx series (Cu-rich). The 2xxx alloys possess outstanding mechanical properties, with AA2024-T3 being one of the most used alloys in the aerospace industry due to its high specific strength [1, 2]. However, due to its Cu-rich inter-metallic phases (IMP), AA2024-T3 is highly susceptible to various forms of corrosion [3], such as pitting corrosion, stress-corrosion cracking, and galvanic corrosion [4], which can compromise structural integrity and performance. Studies have shown that corrosion accounts for a considerable portion of maintenance costs and downtime in aerospace, with estimates indicating annual global costs exceeding \$2.5 trillion [5].

Preventive measures and proactive decisions, such as scheduling maintenance or assessing corrosion stages, often rely on properties measured at the macroscopic level, such as chemical concentrations or the formation of byproducts. These observations are typically derived from experimental data and are frequently supported by computational models capable of accurately describing the entire corrosion process. A common approach to developing computational models for corrosion involves addressing its inherently multi-scale nature by decomposing the problem into distinct levels. At the atomistic scale, the focus lies on capturing the fundamental chemical reactions occurring within the system, while the mesoscopic and macroscopic scales are typically modeled using finite volume (FVM) or finite element methods (FEM) to describe larger-scale behaviors and interactions [6].

Over the years, FVM or FEM have been used significantly to model corrosion in several systems, shedding light on corrosion progression, surface passivation mechanisms, and strategies for guiding corrosion inhibition [7–11]. The accuracy of FVM and FEM depends heavily on how well the kinetic rate of the chemical reactions at the alloy surface and within the electrolytes are quantified, given their coupled nature. While some parameters can be reliably estimated through well-established experimental techniques, others are barely accessible and often require highly complex and expensive experimental equipment. This challenge is particularly evident for the oxygen reduction reaction (ORR, $\text{O}_2 + 4\text{e}^- \rightarrow 2\text{O}^{2-}$), whose kinetic rate is notoriously difficult to measure experimentally.

In 2xxx alloys, the ORR plays a critical role as the cathodic half-reaction of the overall redox process. This reaction is catalyzed by the IMPs, which transform into nearly pure Cu-rich spots in the early stages of corrosion [12], see Fig 1A. The ORR is initiated once the oxygen dissolved in solution undergoes reductive adsorption on the IMP surface ($\text{O}_{2(\text{g})} + \text{e}^- \rightarrow \text{O}_{2(\text{a})}^-$), forming the superoxide ion which then undergoes to a reductive dissociation ($\text{O}_{2(\text{a})}^- + \text{e}^- \rightarrow 2\text{O}_{(\text{a})}^-$) as shown in Fig. 1A reaction 1 and 2, respectively. After, further reduction of the O^- ions (reaction 3) complete the ORR cycle with a total extraction of 4e^- from the metal surface. While the steps 1-3 take place at the IMP, the difference in the Nernst potential results in a spontaneous electron transfer between the Cu-rich IMP and the aluminum matrix, which is in turn oxidized. The oxidation of the aluminum is the main driver for the visible degradation of the alloy surface, *e.g.*, pitting corrosion, which compromises its mechanical properties over time.

Given the multi-electron transfer pathways and the presence of reactive intermediates illustrated in Fig. 1B, it is unsurprising that the ORR is very challenging to evaluate experimentally. Fortunately, atomistic simulations offer an ideal computational toolbox for calculating these kinetic rates *in silico*, providing mechanistic insights and serving as a powerful tool to investigate how environmental conditions and alloy composition affect reactivity [13]. In this context, a substantial body of research has focused on modeling the ORR on various metals and alloys using classical quantum chemistry [14–17]. More recently, also hybrid approaches that combine quantum chemistry methods with both classical and quantum computing have been applied in material science [18–20], including studies that can may be relevant to corrosion, such as the dissociation of water on a magnesium surface [21].

In this work, we present, for the first time, a hybrid quantum computing workflow to model the reductive dissociation of oxygen at the molecular level on a copper slab, simulating the processes occurring on Cu-rich aluminum alloys (AA). Specifically, in section 2.1 and 2.2, we employ density functional theory (DFT), Hartree-Fock (HF) and post-HF methods to identify the critical geometries and the reaction pathways, determining the activation energies and kinetic rates while establishing a reference for strong correlation effects. In section 2.3, we use this results to construct an embedding Hamiltonian for quantum simulations where we employ the variational quantum eigensolver (VQE) and quantum phase estimation (QPE) algorithms to solve the electronic structure problem and benchmark their performance and runtime. Finally, we

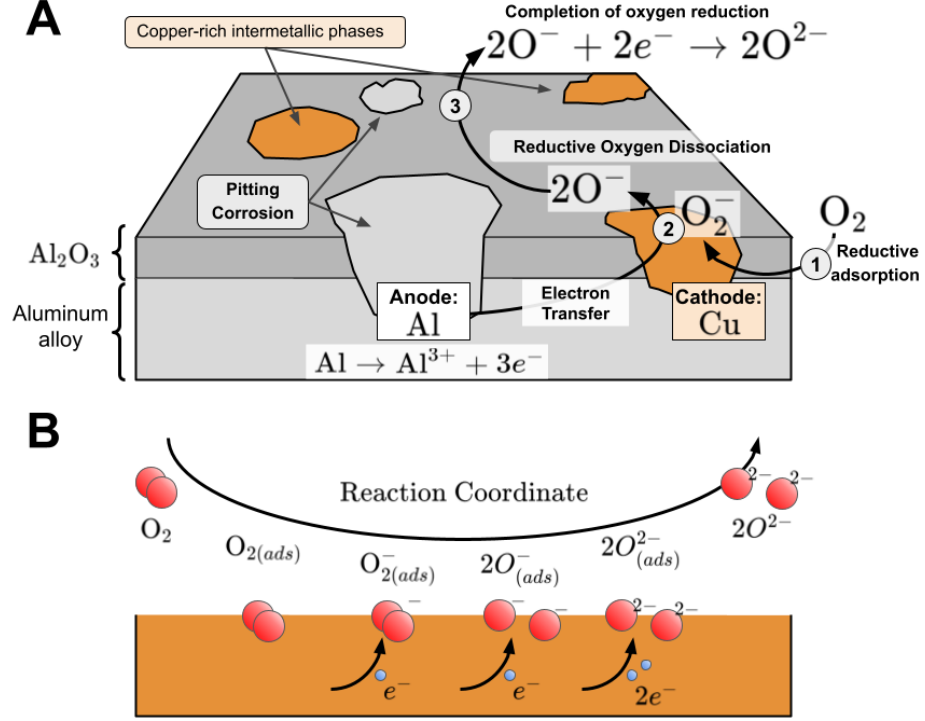


Fig. 1 (A) Schematic representation of the AA2024 microstructure and the ORR chain. The ORR involves three key steps: 1) Reductive adsorption of molecular oxygen onto the Cu-rich IMP, 2) reductive dissociation of oxygen molecules, 3) completion of the oxygen reduction reaction through further reduction of oxygen ions to form oxo-ions. This reduction sequence drives the oxidation of the aluminum matrix, ultimately leading to macroscopic corrosion phenomena. (B) Close-up view of reactions 1 to 3, detailing the transformation from molecular oxygen to oxo-ions on Cu substrate.

conclude by discussing the implications of these results for the feasibility of quantum approaches in modeling chemical processes of practical importance, such as corrosion.

2 Results and Discussion

The kinetic rate of a chemical reaction (k) can be calculated using the standard transition state (TS) theory [22, 23] via Arrhenius law $k = Ae^{-E_a/(RT)}$, where A is the frequency factor, representing the frequency of collisions between reacting molecules and E_a is the activation energy. R is the universal gas constant and T is the absolute temperature. E_a corresponds to the minimum energy required for a reaction to occur, representing the energy barrier that the system must overcome along the reaction pathway. In this work, we focus on the reductive dissociation reaction path taking place after the oxygen molecule has adsorbed onto the alloy surface (reaction 2 in

Fig. 1A). This choice is motivated by two factors: (i) We anticipate this reaction to be the bottleneck of the overall oxygen reduction reaction (ORR), *i.e.*, the step with the highest energy barrier that governs the overall reaction rate, and (ii) we speculate that this pathway include strong correlation effects due to the electron transfer that alter the electronic character of the ground state and therefore suitable to be studied using quantum computing approaches.

2.1 The electronic nature of the reductive dissociation

To map the reductive dissociation reaction path, we use a simplified model representing Cu-rich IMPs. This model is described as a pure copper supercell, with periodic boundary conditions applied in the in-plane directions and a vacuum imposed in the direction perpendicular to the adsorption sites. Using this supercell, we optimized three critical geometries (Fig. 2A). These geometries are as follows: the reactant configuration, where the molecular oxygen is adsorbed on the copper supercell, and the two possible product configurations (*cis* and *trans*).

Using these three geometries, we trace the reaction profile by employing the nudged elastic band (NEB) with DFT (see Supporting Information for more details), which generates a series of interpolated geometries between the initial and final states, including approximate TS geometries for each reaction step. In this case, we identify two transition states: The first one connects the reactant and the *cis* configuration and is associated with the reductive dissociation reaction itself (TS_{diss}), while the second one connects the *cis* and *trans* configurations, corresponding to the diffusion of the two oxygen ions across the supercell slab (TS_{diff}).

2.1.1 Density of States at Reactant Geometry

Next, we focus on identifying the electronic nature of these five geometries. We begin by analyzing the projected density of states (PDOS) over three sets of atomic orbitals: oxygen 2p (O(2p)), copper 3d (Cu(3d)), and copper 4s (Cu(4s)), as shown in Fig. 2B for each of the five geometries. Starting with the reactant, our attention is on the position of the electronic bands projected onto the O(2p) orbitals, specifically those with $\pi^*(\text{O}-\text{O})$ and $\sigma^*(\text{O}-\text{O})$ character. The $\pi^*(\text{O}-\text{O})$ bands are located near the Fermi energy (highlighted in yellow) and, compared to free molecular oxygen, are split into parallel and perpendicular components due to the interaction with the metal surface, resulting in the loss of degeneracy. The two components can be disentangled by plotting the integrated densities in two energy windows: The $[1, 0]$ eV windows is associated with π_{\perp}^* orbital while the $[-1, 0]$ eV range is mostly characterized by the π_{\parallel}^* orbital, as shown in Fig. 2C. In contrast, the $\sigma^*(\text{O}-\text{O})$ (see panel C) band lay in the $[4.2 - 1.5]$ eV energy window (highlighted in red) above the Fermi energy, indicating that it remains fully unoccupied.

Remarkably, at the reactant stage, integrating the PDOS over the two oxygen atoms reveals an excess electron density on the oxygen molecule of approximately one electron. This suggests that, as mentioned earlier, the oxygen molecule has already accepted one electron during the adsorption process, resulting in the formation of a superoxide ion (O_2^-).

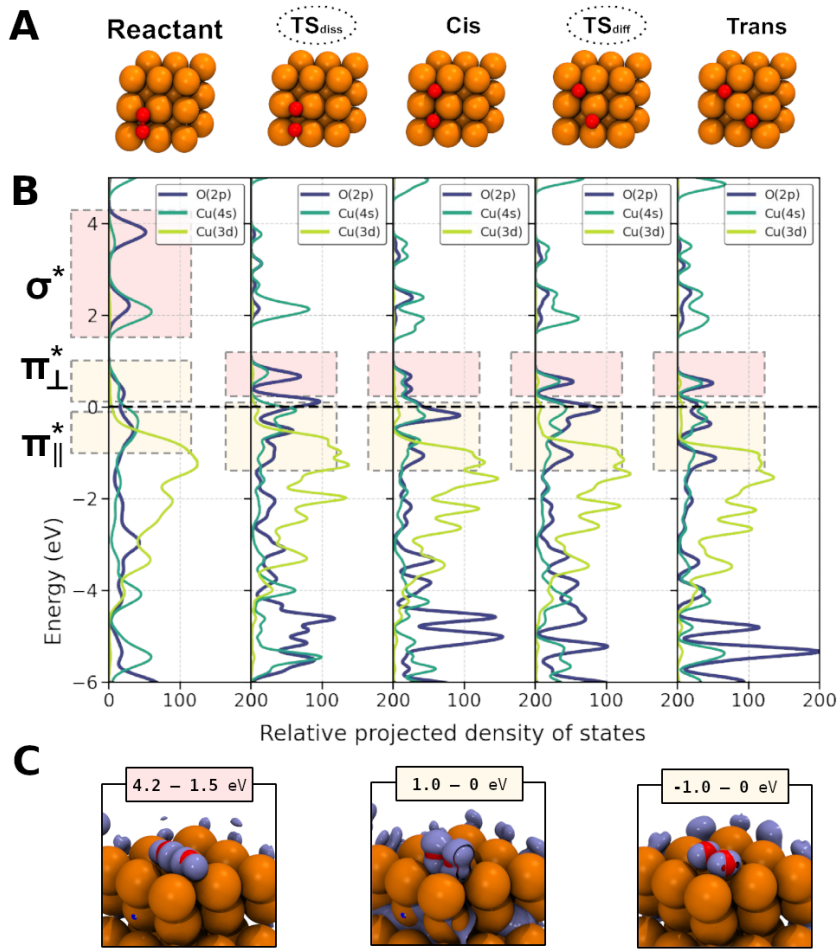


Fig. 2 (A) top view of geometries identified along the reaction pathway: reactant, oxygen dissociation (TS_{diss}), *cis* configuration, oxygen diffusion (TS_{diff}) and *trans* configuration. (B) PDOS for each one of the five geometries in A; we show those levels relevant for the oxidation: O(2p) in blue, Cu(4s) green and Cu(3d) yellow. Regions associated to molecular orbitals σ^* and π^* (parallel and perpendicular to the surface) are highlighted in light red and yellow respectively. (C) Graphical representation of the charge distribution integrated over [4.2 – 1.5] eV, [1.0 – 0] eV and [-1.0 – 0] eV energy windows at the reactant geometries.

2.1.2 Density of States at Transition State

Examining the $\pi^*(\text{O}-\text{O})$ and $\sigma^*(\text{O}-\text{O})$ bands at TS_{diss}, we observe that all of them shift towards lower energies, with the $\sigma^*(\text{O}-\text{O})$ band now approaching the Fermi energy level. This shift is a clear indication that the electronic character of the molecular system is changing: Electron transfer is occurring from the metal surface to the molecular oxygen. As the distance between the two oxygen atoms increases, the

$\sigma^*(\text{O}-\text{O})$ band becomes strongly stabilized, promoting the second electron transfer, resulting in the accumulation of approximately two excess electrons, one on each oxygen atom. The stabilization of the $\sigma^*(\text{O}-\text{O})$ band further reduces the bonding energy of the superoxide ion, weakening the O–O bond and favoring the dissociation process.

Finally, we conclude by observing that no additional electron transfer occurs once the *cis* product is formed, as indicated by the minimal changes in the PDOS profile beyond this point. The second segment of the reaction path, therefore, represents a purely diffusive process of the oxygen atoms across the copper lattice, with little to no impact on the electronic structure of the molecular system.

2.2 Energy Profiles along the Reaction Path

The change on electronic character occurring at the TS_{diss} geometry has significant implications for the energy profile along the reaction pathway. To understand this, we use the set of five geometries (Fig. 2A), along with the interpolated geometries generated via the NEB technique using DFT, to compute with HF and post-HF methods the relative electronic energy along the reaction path, as shown in Fig. 3A. We calculate the energy profile using DFT with the Perdew-Burke-Ernzerhof (PBE) exchange-correlation functional [24] (yellow) and HF (light green). HF predicts a significantly higher energy barrier than DFT and shows the energy basins not centered at the *cis* and *trans* products. However, these discrepancies are not surprising as the geometries were optimized using PBE, which leads to suboptimal bond distances for HF. Moreover, the treatment of electronic interactions in DFT and HF differs significantly. In fact, HF is entirely incapable of accounting for both static correlation – which occurs when multiple electronic configurations contribute to the ground state (multiconfigurational character) – and dynamic correlation, related to orbital relaxation. In contrast, DFT can accurately describe dynamic correlation with a suitable functional [25, 26].

2.2.1 Static Electron Correlation along the Reaction Path

To include static correlation in the HF wavefunction, a common approach is to employ configuration interaction (CI). In CI, additional electronic configurations are introduced by generating excitations from the reference HF wavefunction. Electrons are excited from occupied orbitals in the reference configuration to unoccupied ones, producing single, double, and higher excitations. These excited configurations can significantly contribute to the description of the electronic ground state marking the ground state as multiconfigurational. To make this process computationally efficient, the excitations are restricted to a subset of orbitals called the active space (AS). The AS defines the most relevant orbitals involved in the chemical reaction. In this study, the AS is constructed using the Atomic Valence Active Space (AVAS) method [27]. AVAS projects the HF molecular orbitals (MOs) onto an atomic orbital (AO) subspace, localizes and computes the overlap between them, and selects the most important orbitals on the basis of this overlap. Due to the nature of the reductive dissociation reaction, we choose the AO subspace comprising the 2p orbitals of oxygen and the 3d

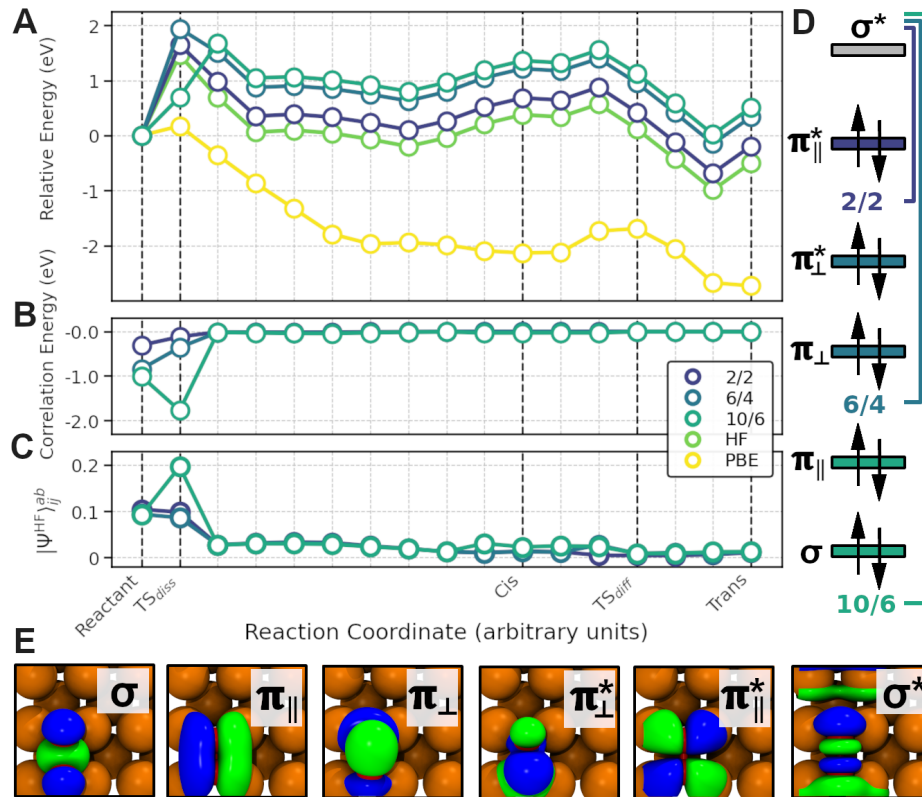


Fig. 3 Energy and electronic correlation profiles along the reaction pathway. (A) Relative energy profiles calculated using DFT (PBE), HF, and FCI for active spaces (2/2) in purple, (6/4) in blue-green and (10/6) in green. (B) Correlation energy differences between FCI and HF along the reaction path. (C) Largest contribution of the doubly excited determinant appearing in the FCI wavefunction. (D) Schematic representations of three active spaces used in calculations. (E) Visualization of the HF molecular orbitals sketch in D for the reactant geometry. The labels are based on the largest contribution from the oxygen atomic orbitals.

orbitals of copper. As already shown in Fig. 2B, this AO subspace is critical since it is directly involved in the electron transfer.

With the AS defined, we proceeded to compute the energy using the full configuration interaction (FCI) method, where all possible excitations are generated within the AS. We performed this calculation for three different active spaces: (2/2) in purple, (6/4) in dark green, and (10/6) in green (see Fig. 3D and Fig. 3E where we represent the diagrams and graphical representation of the orbitals of the AS, respectively). The resulting energy profiles are shown in Fig. 3A. It is important to note that, in all three active spaces, we included only one virtual orbital – the $\sigma^*(\text{O}-\text{O})$, which is associated with the bond-breaking orbital in the reductive dissociation of O_2 . As a result, the maximum degree of excitations that can be generated from the

HF configuration is two-electron excitations.

From the comparison of these three profiles with the HF energy profile, we observe a significant variation in both the energy barrier and the relative energies of the products compared to the reactants. In fact, for the two largest active spaces, (6/4) and (10/6), the thermodynamic driving force is even reversed, with the products being higher in energy than the reactants. This suggests that electron correlation plays an important role along the reaction pathway. To pinpoint where correlation effects are most significant, we plotted the energy difference between the FCI and HF calculations at each point along the reaction path (Fig. 3B). The correlation energy is more negative for the reactants and the TS_{diss} , while it becomes negligible for the remainder of the path. In other words, the initial section of the reaction path is characterized by an electronic ground state with a strong contribution from excited configurations. As seen in Fig. 3C, which shows the largest coefficient of the doubly excited state determinant in the FCI vector, the initial portion of the reaction path exhibits a strong contribution from doubly excited state determinants, responsible for the large correlation energy observed.

The appearance of multiple excited state determinants in the ground state at the reactant and TS_{diss} geometries suggest that the usage of quantum computer to model this reactions maybe appropriate. With the AS already defined, we can easily construct an embedding Hamiltonian that explicitly describes the electrons within the reduced Fock space spanned by the AS orbitals [28], treating the remaining electrons as an average, effective one-body interaction (see section SI1 of Supporting Information for more details). The selected electronic Hamiltonian, specific to each active space and geometry, is then transformed using the Jordan-Wigner method to prepare it for quantum computation.

2.3 The Electronic Problem using a Quantum Computer

At this point, our discussion focuses on determining the static correlation contribution, as shown in Fig. 3B, using a quantum computing framework, alongside an analysis of the associated resource requirements. Our goal is to provide a clear understanding of the resources needed to run both the VQE algorithm, designed for near-intermediate scale quantum (NISQ) computers, and a standard QPE algorithm [29, 30], suitable for fault-tolerant quantum computers (FTQC).

To present this comparison, we compiled the VQE quantum circuit (details of the calculation are provided in section 4) on a fake backend with `Clifford+T` set of basis gates and all-to-all connectivity. We compiled circuits for the three active spaces previously described, as well as for additional spaces, namely (14/8), (18/10), and (22/12), to highlight the asymptotic scaling of the algorithm with increasing embedding Hamiltonian size. For each active space, we plotted the number of two-qubit gates associated with the circuit and the runtime per each ansatz run with numerical values assigned to parameters (either for gradients evaluation or energy estimation for parameters), computed naively as the circuit depth multiplied by the “clock time” of the backend described in details in section SI3. The results for the number of two-qubit gates and runtime (in minutes) as functions of the circuit depth are shown as

empty stars in the panel A and C of Fig. 4, respectively. It is important to note that for VQE, the runtime also include the multiplication by number of shots.

To account for backend noise, we present the runtime with quantum error correction (QEC) applied using the surface code using the quantum resource estimation tool provided by Microsoft Azure Quantum [31, 32]. Further details about the quantum error correction parameters used are provided in section SI3.

For VQE without QEC estimated runtime goes subminutes, allowing for effective VQE run. For QEC results, we observe systematic increase in runtime by around two orders of magnitude. That’s significant increase, crossing the one minute barrier per experiment for over than 8 spin orbitals active spaces. That values makes VQE unfeasible to run, particularly for active spaces expensive to run classically (20+ spin orbitals). On top of that, the all-to-all connectivity might be unrealistic assumption even for logical qubits at future architectures. For thousands of physical qubits sparser connectivity adds the overhead, which no longer can be ignored.

At this point, we turn our attention to the QPE calculation, compiled on the same backend used for VQE, applied to the two smallest active spaces, namely (2/2) and (6/4). We note in passing that, for simulation purposes, the QPE calculation for the (6/4) active space was performed with only 10 ancilla qubits, which is fewer than the number required to achieve chemical accuracy precision for storing the phase (see section SI1, Fig. SI3).

As expected, the circuit depth and the number of two-qubit gates required to execute the QPE algorithm are substantially higher than those for VQE. Comparing the results in panels A and B of Fig. 4 for the (6/4) active space, the VQE algorithm has a circuit depth of 2×10^3 and requires 10^3 two-qubit gates. In contrast, the QPE algorithm exhibits a circuit depth that is five orders of magnitude larger and involves four orders of magnitude more two-qubit gates. Despite this disparity, the runtime for QPE without QEC overhead (empty stars panel E) is comparable to that of VQE (empty stars in panel C), primarily due to the unfavorable scaling of the number of shots required in VQE. However, when we consider the QEC overhead, we see a much larger penalty for QPE than VQE due to the significant circuit depth of the QPE algorithm. As shown in Fig. 4E, the runtime for QPE increases by nearly three orders of magnitude when comparing the results with QEC (full stars) and the runtime without QEC (empty stars).

For practical applications of QPE, a QEC procedure is, of course, needed. Even under our optimistic assumptions for physical qubit parameters (see section SI3), the runtime for the relatively small (6/4) active space is approximately 6 minutes with error correction. This runtime is significantly longer than the sub-millisecond runtime achievable through exact diagonalization on a classical computer. Moreover, since the QPE algorithm provide only a polynomial advantage with respect to classical methods – due to the exponential reduction of the overlap between the HF wavefunction and the true ground state [33] – QPE is unlikely to offer significant benefits in finding the real ground state (at least for Hamiltonian of small/medium sizes).

To complete future scenario with applicable QEC, let’s consider quantum hardware with parameters exceeding specifications used so far. This scenario is illustrated in

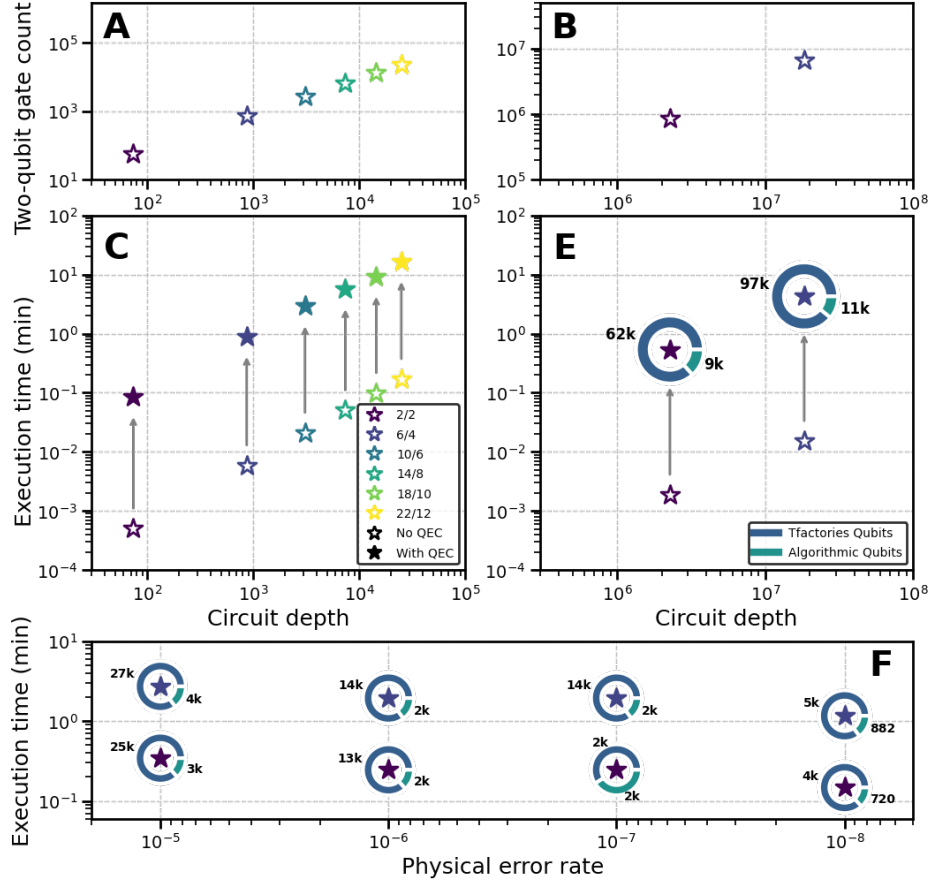


Fig. 4 (A)-(B) Two-qubit gate counts for the VQE and QPE calculations, respectively. The color gradient, transitioning from purple to yellow, represents the different active spaces used, ranging from (2/2) in purple to (22/12) in yellow. All estimations were performed for a fully connected generic backend (V2) provided by Qiskit. Empty stars denote calculations without QEC, while full stars include QEC estimates based on the surface code. (C)-(D) The runtime of the algorithm for each embedded Hamiltonian in the VQE and QPE calculations. In panel (E), the number of physical qubits required to run the algorithm, including those for T-state preparation, is plotted. Finally, (F) illustrates the dependency of estimated execution runtime and the number of physical qubits on physical qubit error rates of QPE algorithm.

Fig. 4F, where the runtime and the number of physical qubits required are plotted against the qubit physical error rate, ranging from 10^{-5} to 10^{-8} . Even under such optimistic – and perhaps improbable – engineering advancements, as expected, the number of qubits required decrease drastically dropping from 31 thousands at 10^{-5} error rate to less than 6 thousands for 10^{-8} error rate. On the other hand, the QPE execution runtime, which is closely tied to the surface code logical cycle, does not

chance substantially. As a result, QPE still appears impractical without substantial improvements in both algorithms and QEC techniques.

Some of these improvements are already available today, including qubitization [34], quantum walk operators [35, 36], approximation of the electron repulsion tensor [37], and more efficient error correction schemes [38]. Still, these advancements may not be sufficient to make QPE competitive. In light of these results, it is clear that optimization of physical qubit specifications is not the only variable required to make quantum computing useful for business-relevant applications but more effort has to be devoted to algorithmic innovations.

Finally, the number of physical qubits required, as shown in Fig. 4E, also seems concerning. The $\sim 110k$ qubit required to run the QPE for the $(6/4)$ active space – primarily driven by the demands of T-factory distillation – pose a significant bottleneck. For context, Quantinuum anticipates building its Apollo chip by 2029 with “only” 1,000 physical qubits and a two-qubit error rate of 10^{-4} , consistent with the error rate assumptions in our analysis. The fact that quantum computing, at least for chemistry applications, is a distant prospect is perhaps unsurprising. However, our analysis underscores just how far we are from realizing any tangible industrial benefits from quantum computing, especially given that much larger Hamiltonians will need to be addressed before meaningful advantages can be achieved.

3 Conclusion

To the best of the authors’ knowledge, this study represents the first comprehensive investigation of corrosion processes using a hybrid workflow that integrates both NISQ-oriented algorithms and fault-tolerant quantum computing approaches. We focused on one of the initial steps of the corrosion process: The ORR on a copper surface, a reaction that characterizes the corrosion of Cu-rich AA and which is of paramount importance for the oxidation of the aluminum substrate.

The present study was divided into two critical steps. The first step involved assessing the ORR rate, which is essential for constructing macroscopic models of the reaction. This was achieved using classical quantum chemistry methods, including DFT, HF, and post-HF methods. This analysis revealed and quantified the activation energy barrier for the reaction while also highlighting the emergence of a strongly correlated ground state caused by a change in the electronic structure’s nature. This finding is particularly significant because strongly correlated states are notoriously challenging for conventional classical methods, whereas quantum computers could offer a distinct advantage in handling them.

Armed with these insights, the attention was turned to the VQE and QPE quantum computing algorithms. Specifically, the resources required to perform such calculations on a quantum device was analyzed. Unsurprisingly, the estimates for VQE with QEC reach a few minutes per iterations, due to surface code overhead and significant number of shots. VQE may requires thousands up to millions of single circuit runs, depending of number of parameters in the ansatz, that’s why small runtime of single experiment

execution is crucial. Naturally, current IBM’s backends have heavy-hex architectures, which makes real-backend transpiled circuits laid out on 1D chain of qubits, increasing number of gates and circuit depth few times. This highlight the need of optimizing VQE towards faster convergence to ground state energy with less iterations and with shallower circuits plus working on increasing the quality of quantum backends, even with QEC applied, to make VQE feasible on real hardware with 20 or more qubit.

On the other hand, while QPE is expected to scale more favorably (polynomially with respect to the active space size), it suffers from the considerable overhead associated with QEC, imposing substantial penalties on both qubit count and runtime. Even under optimistic assumptions regarding physical qubit characteristics, the resource demands for QPE remain far from competitive with classical methods for the active space sizes explored here – and likely for larger active spaces as well. Furthermore, even with significant improvements in physical qubit error rates, while the required number of qubits decreases significantly, the same cannot be said for execution runtime.

In light of these findings, it has been concluded that improvements in physical qubit hardware alone are insufficient to make quantum computing viable, at least for finding the ground state of molecular systems. Instead, substantial advancements in algorithm design and QEC procedures are essential to make quantum computing useful in the domain of material science.

Implementing algorithmic improvements to assess how far the estimated resource requirements can be reduced for this specific problem and to evaluate the threshold at which quantum computers may outperform their classical counterparts are inevitable and will be subject of future works. Furthermore, the investigation of the reductive adsorption process through dynamic simulations holds promise. We anticipate that these simulations could reveal vibrational and electronic coupling phenomena, potentially paving the way for simulating the full molecular wavefunction on a quantum computer.

4 Methods

Quantum Chemistry Electronic Structure. All DFT calculations (SCF and NEB calculations) were performed using the Quantum ESPRESSO 7.3 [39–41]. The PBE exchange-correlation functional [24] were utilized within the generalized gradient approximation (GGA). We used ultra-soft pseudopotentials for copper and oxygen to efficiently represent electron-ion interactions while maintaining computational efficiency.

The system was modeled as a three-layer slab of copper with a 3×3 arrangement of atoms in each layer, exposing a surface of the crystal plane (001). The slab was constructed with a 30 Å vacuum along the z axis with a O₂ molecule placed on the surface. The molecular orbitals occupations were treated with Gaussian smearing using a smearing width of 0.01 Ry to facilitate convergence of metallic states. The electronic self-consistency was controlled by a local Thomas-Fermi mixing mode. A plane-wave kinetic energy cutoff of 50 Ry and a charge density cutoff of 200 Ry were applied based on convergence tests and the Brillouin zone was sampled at the Gamma point.

The structural relaxations, including the optimization of the reactants and product as well as the NEB simulations, were performed until the forces on each atom were below 0.01 eV/Å, with the electronic convergence threshold set to 10^{-8} eV.

For electronic structure analysis, the projected density of states (PDOS) was calculated by projecting the Kohn-Sham states onto atomic orbitals, using a Gaussian smearing width of 0.02 Ry. The Fermi energy was set at zero for convenience in plotting PDOS data.

The HF wavefunction was obtained using PySCF 2.6.2, employing Gaussian-type orbitals as the basis set, with basis functions having exponential coefficients smaller than 0.1 discarded, along with an auxiliary basis set for density fitting. The slab structure optimized with DFT was modified by removing the bottom layer of copper atoms, resulting in a two-layer copper slab. To ensure consistency, the same kinetic energy cutoff and periodic boundary conditions used in the DFT calculations were applied to the HF calculations. The HF molecular orbitals (MOs) were subsequently utilized for correlated (post-HF) calculations and to construct the embedding Hamiltonian, which incorporates effective one- and two-body interactions [28]. The embedded Hamiltonian expressed in second quantization was transformed as qubit operator by Jordan-Wigner mapping.

Quantum Computing. The VQE is a heuristic hybrid quantum-classical algorithm for finding the ground and excited state energies of a quantum Hamiltonian [42]. In this work the method resolving ground state estimation problem was applied. This approach is based on the Ritz variational principle [43], where by expressing the simulated system state through the parametrized quantum state $\Psi(\theta)$ on a quantum circuit, the lowest energy configuration is sought through tuning the parameters θ towards the ground state energy E_0 :

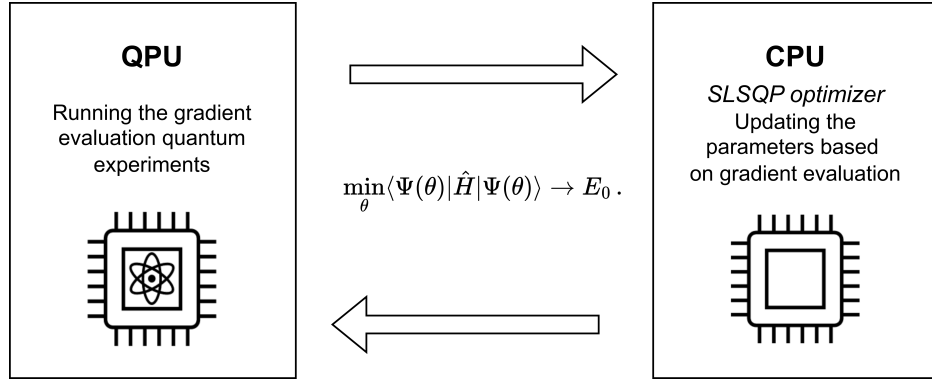


Fig. 5 Schematic representation of VQE computational flowchat.

The VQE routine was implemented with Qiskit 1.2 [44]. Number of shots was set up on 8192, also for resource estimation. The unitary coupled cluster with singles and doubles (UCCSD) ansatz was used, based on the selected active space and the initial state based on the HF wavefunction. UCCSD yields deep circuits in comparison to other methods (*e.g.*, hardware efficient ansatz), but is chemistry-informed and has fewer parameters, because the terms exponentiated in the ansatz are grouped and often share the same parameter. Detailed comparison of the depths and number of parameters per different ansatzes in section SI2. The energy was measured with a qubit mapped effective Hamiltonian of reactant in second quantized form. As an optimizer SLSQP [45] was used, due to its good empirical performance for VQE [46, 47]. Additionally, Adapt-VQE, truncation of terms in UCCSD, and Clifford parameters warm start were tested with no improvements in accuracy and number of iterations was observed. All the resource estimation results were generated for a generic implementation with built-in Qiskit 1.2 transpilation options with `optimization_level=1` and `ElidePermutations` pass included. The VQE converged towards analytically calculated ground state energies for three checked active space sizes: (2/2), (6/4) and (10/6). The results are shown in section SI2 at Figure SI4.

The QPE algorithm was implemented using Qiskit 1.2 [44]. The Hamiltonian was scaled by a factor ϵ to ensure that the corresponding phase readout, $\phi_i \equiv 2\pi\lambda_i$ with $\{\lambda_i\}$ the eigenspectrum of the Hamiltonian, lies within the interval $\in (0, 2\pi]$ (see section SI1). Specifically, $\epsilon = 0.8$ a.u. and $\epsilon = 3.91$ a.u. were used for the embedding Hamiltonian in the (2/2) and (6/4) active spaces, respectively. These values were selected somewhat arbitrarily to be slightly higher than the modulus of the largest eigenvalue of the two operators. It is worth noting that this is not the most efficient method to extract the phase after running the QPE algorithm, as the resulting phases may not correspond to the closest discrete binary representation. However, we believe this approach is valid for practical applications of QPE, where the eigenspectrum of the Hamiltonian can only be inferred approximately, and the full spectrum is not known. The full eigenspectra of the (2/2) active space is shown in Fig. SI1.

The exponentiated Hamiltonian was approximated using the Lie-Trotter formula, with the accuracy of the approximation monotonically improving as the number of Trotter repetitions increased. We determined that 3 and 1 Trotter steps, along with 10 and 13 ancilla qubits, were sufficient to achieve chemical accuracy for the (2/2) and (6/4) active spaces, respectively (see Fig. SI2 and Fig. SI3).

Supplementary information. Supporting Information is available free of charge.

Acknowledgements. We acknowledge the valuable insights provided by Walden Killick and James Cruise from Cambridge Consultants during discussions on quantum error correction analysis. We also extend our gratitude to the Surface and Technology team at Airbus AIRTeC (Bristol, United Kingdom), particularly Jeremy Bradley (Senior Expert in Surface Protection and Corrosion Prevention), for their support and contributions to this project. Finally, we are deeply grateful to Airbus and Capgemini for fostering an excellent work environment focused on innovation and technological advancement.

Declarations

Competing interests. The authors declare no competing interests.

Data availability. The authors declare that the data supporting the findings of this study are available within the main article and the Supplementary Information. Additional data are available from the corresponding author upon request.

Author contributions. E.M. and R.B. conceived the project. R.B. defined the use case and underlying simplifications. E.M. and J.M.A.H. designed the classical chemistry calculations and analyzed the data. E.M. developed the embedding Hamiltonian formulation and performed the QPE calculations. M.K. and L.R. performed the VQE calculations. All authors contributed to writing and reviewing the manuscript.

References

- [1] Rambabu, P., Eswara Prasad, N., Kutumbarao, V., Wanhill, R.: Aluminium alloys for aerospace applications. *Aerospace materials and material technologies: volume 1: aerospace materials*, 29–52 (2017)
- [2] Jegdić, B., Bobić, B., Linić, S.: Corrosion behaviour of aa2024 aluminium alloy in different tempers in nacl solution and with the cecl3 corrosion inhibitor. *Materials and Corrosion* **71**(3), 352–364 (2020)
- [3] Abodi, L.-C., Derose, J., Van Damme, S., Demeter, A., Suter, T., Deconinck, J.: Modeling localized aluminum alloy corrosion in chloride solutions under non-equilibrium conditions: Steps toward understanding pitting initiation. *Electrochimica Acta* **63**, 169–178 (2012)
- [4] Frankel, G., Sridhar, N.: Understanding localized corrosion. *Materials today* **11**(10), 38–44 (2008)
- [5] Koch, G., Varney, J., Thompson, N., Moghissi, O., Gould, M., Payer, J.: International measures of prevention, application, and economics of corrosion technologies (impact) study (nace international, houston). Available at impact.nace.org/documents/Nace-International-Report.pdf. Accessed March 6, 2019 (2016)
- [6] Gunasegaram, D., Venkatraman, M., Cole, I.: Towards multiscale modelling of localised corrosion. *International materials reviews* **59**(2), 84–114 (2014)
- [7] Xiao, J., Chaudhuri, S.: Predictive modeling of localized corrosion: An application to aluminum alloys. *Electrochimica Acta* **56**(16), 5630–5641 (2011)
- [8] Murer, N., Missert, N., Buchheit, R.: Finite element modeling of the galvanic corrosion of aluminum at engineered copper particles. *Journal of The Electrochemical Society* **159**(6), 265 (2012)

- [9] DeRose, J.A.: Aluminium Alloy Corrosion of Aircraft Structures: Modelling and Simulation. WIT press, ??? (2013)
- [10] Duddu, R., Kota, N., Qidwai, S.M.: An extended finite element method based approach for modeling crevice and pitting corrosion. *Journal of Applied Mechanics* **83**(8), 081003 (2016)
- [11] Saeedikhani, M., Blackwood, D.J.: Finite element method for thin film corrosion modelling: Where we advanced and where we would like to advance? *Corrosion and Materials Degradation* **1**(2), 273–281 (2020)
- [12] Kosari, A., Tichelaar, F., Visser, P., Zandbergen, H., Terryn, H., Mol, J.: Dealloying-driven local corrosion by intermetallic constituent particles and dispersoids in aerospace aluminium alloys. *Corrosion Science* **177**, 108947 (2020)
- [13] Exner, K.S., Over, H.: Kinetics of electrocatalytic reactions from first-principles: a critical comparison with the ab initio thermodynamics approach. *Accounts of chemical research* **50**(5), 1240–1247 (2017)
- [14] Chu, S., Bovi, D., Cappelluti, F., Orellana, A.G., Martin, H., Guidoni, L.: Effects of static correlation between spin centers in multicenter transition metal complexes. *Journal of Chemical Theory and Computation* **13**(10), 4675–4683 (2017)
- [15] Liu, G., Liu, Z., Ao, B., Hu, W., Deng, H.: Oxygen adsorption and diffusion on γ -u (0 0 1) surface: effect of titanium. *Computational Materials Science* **144**, 85–91 (2018)
- [16] Ke, H., Taylor, C.D.: Density functional theory: an essential partner in the integrated computational materials engineering approach to corrosion. *Corrosion* **75**(7), 708–726 (2019)
- [17] Li, S., Li, C., Wang, F.: Computational experiments of metal corrosion studies: a review. *Materials Today Chemistry* **37**, 101986 (2024)
- [18] Di Paola, C., Plekhanov, E., Krompiec, M., Kumar, C., Marsili, E., Du, F., Weber, D., Krauser, J.S., Shishenina, E., Ramo, D.M.: Platinum-based catalysts for oxygen reduction reaction simulated with a quantum computer. *arXiv preprint arXiv:2307.15823* (2023)
- [19] Alexeev, Y., Amsler, M., Barroca, M.A., Bassini, S., Battelle, T., Camps, D., Casanova, D., Choi, Y.J., Chong, F.T., Chung, C., *et al.*: Quantum-centric supercomputing for materials science: A perspective on challenges and future directions. *Future Generation Computer Systems* **160**, 666–710 (2024)
- [20] Hariharan, S., Kinge, S., Visscher, L.: Modeling heterogeneous catalysis using quantum computers: An academic and industry perspective. *Journal of Chemical*

- [21] Gujarati, T.P., Motta, M., Friedhoff, T.N., Rice, J.E., Nguyen, N., Barkoutsos, P.K., Thompson, R.J., Smith, T., Kagele, M., Brei, M., *et al.*: Quantum computation of reactions on surfaces using local embedding. *npj Quantum Information* **9**(1), 88 (2023)
- [22] Eyring, H.: The activated complex in chemical reactions. *The Journal of Chemical Physics* **3**(2), 107–115 (1935)
- [23] Bard, A.J., Faulkner, L.R.: *Electrochemical methods: fundamentals and applications*. Surf. Technol **20**(1), 91–92 (1983)
- [24] Perdew, J.P., Burke, K., Ernzerhof, M.: Generalized gradient approximation made simple. *Physical review letters* **77**(18), 3865 (1996)
- [25] Koch, W., Holthausen, M.C.: *A Chemist’s Guide to Density Functional Theory*, 2nd edn. John Wiley & Sons, Weinheim, Germany (2001)
- [26] Grimme, S.: Semiempirical hybrid density functional with perturbative second-order correlation. *The Journal of chemical physics* **124**(3) (2006)
- [27] Sayfutyarova, E.R., Sun, Q., Chan, G.K.-L., Knizia, G.: Automated construction of molecular active spaces from atomic valence orbitals. *Journal of chemical theory and computation* **13**(9), 4063–4078 (2017)
- [28] Battaglia, S., Rossmannek, M., Rybkin, V.V., Tavernelli, I., Hutter, J.: A general framework for active space embedding methods: applications in quantum computing. *arXiv preprint arXiv:2404.18737* (2024)
- [29] Kitaev, A.Y.: Quantum measurements and the abelian stabilizer problem. *arXiv preprint quant-ph/9511026* (1995)
- [30] Nielsen, M.A., Chuang, I.L.: *Quantum Computation and Quantum Information*. Cambridge university press, ??? (2010)
- [31] Beverland, M.E., Murali, P., Troyer, M., Svore, K.M., Hoefler, T., Kliuchnikov, V., Low, G.H., Soeken, M., Sundaram, A., Vasshillo, A.: Assessing requirements to scale to practical quantum advantage. *arXiv preprint arXiv:2211.07629* (2022)
- [32] Prateek, K., Maity, S.: Quantum programming on azure quantum—an open source tool for quantum developers. In: *Quantum Computing: A Shift from Bits to Qubits*, pp. 283–309. Springer, Singapore (2023)
- [33] Lee, S., Lee, J., Zhai, H., Tong, Y., Dalzell, A.M., Kumar, A., Helms, P., Gray, J., Cui, Z.-H., Liu, W., *et al.*: Evaluating the evidence for exponential quantum advantage in ground-state quantum chemistry. *Nature communications* **14**(1), 1952 (2023)

- [34] Low, G.H., Chuang, I.L.: Hamiltonian simulation by qubitization. *Quantum* **3**, 163 (2019)
- [35] Berry, D.W., Kieferová, M., Scherer, A., Sanders, Y.R., Low, G.H., Wiebe, N., Gidney, C., Babbush, R.: Improved techniques for preparing eigenstates of fermionic hamiltonians. *npj Quantum Information* **4**(1), 22 (2018)
- [36] Poulin, D., Kitaev, A., Steiger, D.S., Hastings, M.B., Troyer, M.: Quantum algorithm for spectral measurement with a lower gate count. *Physical review letters* **121**(1), 010501 (2018)
- [37] Rocca, D., Cortes, C.L., Gonthier, J.F., Ollitrault, P.J., Parrish, R.M., Anselmetti, G.-L., Degroote, M., Moll, N., Santagati, R., Streif, M.: Reducing the runtime of fault-tolerant quantum simulations in chemistry through symmetry-compressed double factorization. *Journal of Chemical Theory and Computation* (2024)
- [38] Bravyi, S., Cross, A.W., Gambetta, J.M., Maslov, D., Rall, P., Yoder, T.J.: High-threshold and low-overhead fault-tolerant quantum memory. *Nature* **627**(8005), 778–782 (2024)
- [39] Giannozzi, P., Baroni, S., Bonini, N., Calandra, M., Car, R., Cavazzoni, C., Ceresoli, D., Chiarotti, G.L., Cococcioni, M., Dabo, I., *et al.*: Quantum espresso: a modular and open-source software project for quantum simulations of materials. *Journal of physics: Condensed matter* **21**(39), 395502 (2009)
- [40] Giannozzi, P., Andreussi, O., Brumme, T., Bunau, O., Nardelli, M.B., Calandra, M., Car, R., Cavazzoni, C., Ceresoli, D., Cococcioni, M., *et al.*: Advanced capabilities for materials modelling with quantum espresso. *Journal of physics: Condensed matter* **29**(46), 465901 (2017)
- [41] Giannozzi, P., Baseggio, O., Bonfà, P., Brunato, D., Car, R., Carnimeo, I., Cavazzoni, C., De Gironcoli, S., Delugas, P., Ferrari Ruffino, F., *et al.*: Quantum espresso toward the exascale. *The Journal of chemical physics* **152**(15) (2020)
- [42] Peruzzo, A., McClean, J., Shadbolt, P., Yung, M.-H., Zhou, X.-Q., Love, P.J., Aspuru-Guzik, A., O’Brien, J.L.: A variational eigenvalue solver on a photonic quantum processor. *Nature communications* **5**(1), 4213 (2014)
- [43] Cerezo, M., Arrasmith, A., Babbush, R., Benjamin, S.C., Endo, S., Fujii, K., McClean, J.R., Mitarai, K., Yuan, X., Cincio, L., *et al.*: Variational quantum algorithms. *Nature Reviews Physics* **3**(9), 625–644 (2021)
- [44] Javadi-Abhari, A., Treinish, M., Krsulich, K., Wood, C.J., Lishman, J., Gacon, J., Martiel, S., Nation, P.D., Bishop, L.S., Cross, A.W., *et al.*: Quantum computing with qiskit. *arXiv preprint arXiv:2405.08810* (2024)

- [45] Virtanen, P., Gommers, R., Oliphant, T.E., Haberland, M., Reddy, T., Cournapeau, D., Burovski, E., Peterson, P., Weckesser, W., Bright, J., *et al.*: Scipy 1.0: fundamental algorithms for scientific computing in python. *Nature methods* **17**(3), 261–272 (2020)
- [46] Morita, M., Tomita, Y., Koyama, J., Kimura, K.: Simulator demonstration of large scale variational quantum algorithm on hpc cluster. *arXiv preprint arXiv:2402.11878* (2024)
- [47] Powers, T., Rajapakse, R.: Using variational eigensolvers on low-end hardware to find the ground state energy of simple molecules. *arXiv preprint arXiv:2310.19104* (2023)

Towards quantum utility: Using quantum computing to model corrosion processes

Juan Manuel Aguiar Hualde¹, Marek Kowalik¹, Lian Remme¹,
 Franziska Elisabeth Wolff¹, Julian van Velzen¹, Rene Böttcher²,
 Christian Weimer², Jasper Krauser², Emanuele Marsili^{3*}

¹Capgemini Quantum Lab.

²Airbus, Central Research & Technology, Willy-Messerschmitt-Straße 1,
 Taufkirchen 82024, Germany.

³Airbus, Central Research & Technology, Pegasus House Aerospace Ave,
 Bristol BS34 7PA, United Kingdom.

*Corresponding author(s). E-mail(s): emanuele.marsili@airbus.com;
 Contributing authors: juan-manuel.aguiar-hualde@capgemini.com;
marek-jozef.kowalik@capgemini.com; lian.remme@capgemini.com;
franziska-elisabeth.wolff@capgemini.com;
julian.van.velzen@capgemini.com; rene.boettcher@airbus.com;
christian.weimer@airbus.com; jasper.krauser@airbus.com;

1 Convergence of the Quantum Phase Estimation

The first detail to consider when implementing the Quantum Phase Estimation (QPE) algorithm is the bound of the eigenspectra of the Hamiltonian. Our goal is to map the real eigenvalues, λ_i , to points within the interval $\in (0, 1]$. This ensures that the corresponding phase readouts, $\phi_i \equiv 2\pi\lambda_i$, lie within the interval $\in (0, 2\pi]$. Such a procedure prevents the misassignment of eigenvalues caused by phases wrapping around the 2π range.

For instance, if the smallest eigenvalue of the Hamiltonian is equal to the negative of the largest eigenvalue, it becomes impossible to distinguish these two eigenvalues, as they are mapped to the same point in the interval. To resolve this, we can scale the eigenspectrum of the Hamiltonian by multiplying the operator by a constant factor ϵ such that $\lambda_i \times \epsilon \in (0, 1] \quad \forall \lambda_i$.

A rough estimation of the Hamiltonian's eigenspectrum can be obtained by diagonalizing the Hamiltonian to determine its exact eigenspectrum. Although this implies solving the problem (which defeats the purpose of using the QPE algorithm), it still allows us to extract valuable information, such as the configurations that contribute most to the eigenvectors, including the ground state, and the coefficients associated with each basis state.

In Fig. SI1, we highlight the eigendecomposition of the full Hamiltonian constructed from the active space (2/2), diagonalized over the entire Fock space composed of four fermionic states. The basis states span all possible occupation number vectors, ranging from the empty state $|0000\rangle$ to the fully occupied state $|1111\rangle$. The Hartree-Fock (HF) state corresponds to the $|\text{HF}\rangle \equiv |0101\rangle$ basis state, which can be expressed more explicitly using energy and spin labels for the spin orbitals as $|0_{1,\beta}1_{0,\beta}0_{1,\alpha}1_{0,\alpha}\rangle$, with the two electrons populating the two lowest energy spin-orbitals.

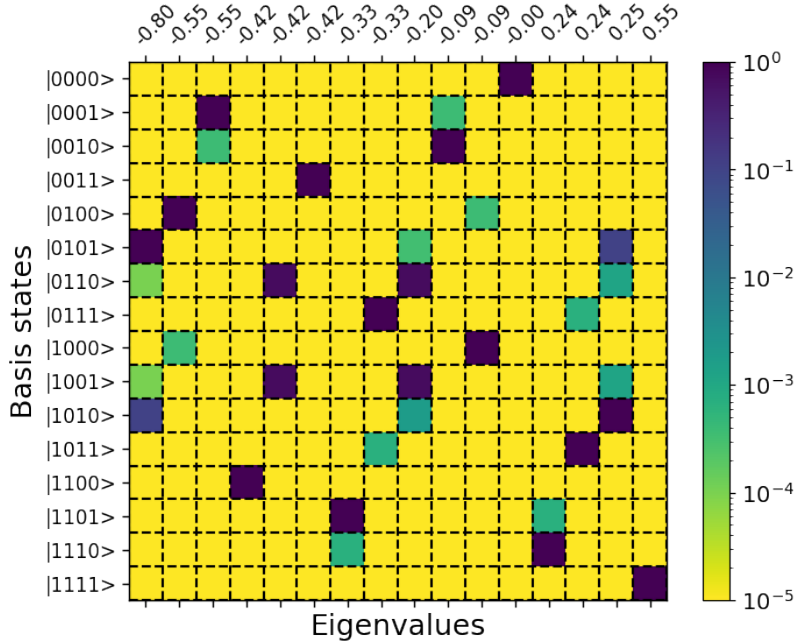


Fig. SI 1 Eigendecomposition of the Hamiltonian diagonalized over the complete Fock space comprising four fermionic states. The eigenvalues are plotted alongside the corresponding eigenvectors, which represent occupation number basis states ranging from the empty state $|0000\rangle$ to the fully occupied state $|1111\rangle$.

For the ground state, which corresponds to the lowest eigenvalue (approximately 0.8 a.u., represented by the leftmost eigenvector), the main contribution comes from

the HF state. However, there is a non-negligible contribution from the doubly excited determinant $|1010\rangle$, which remains a pure single-spin state configuration, as expected, but with two electrons promoted to the $\sigma^*(\text{O}-\text{O})$ orbital. Smaller contributions to the ground state are associated with the singly excited determinants $|1001\rangle$ and $|0110\rangle$. Notably, the triplet electronic states, determined by the determinants $\{|1100\rangle, \frac{1}{\sqrt{2}}(|0110\rangle - |1001\rangle), |0011\rangle\}$, lie higher in energy and are thus considered excited states of the electronic Hamiltonian.

The second key component of the QPE algorithm is the trotterized form of the exponentiated electronic Hamiltonian, $e^{i\mathbf{H}\epsilon}$, where ϵ is the chosen scaling factor. To obtain the Trotterized version of the Hamiltonian, we use the Lie-Trotter formula:

$$e^{i\epsilon \sum_k h_k} \approx \left(\prod_k e^{ih_k \epsilon/n} \right)^n, \quad (1)$$

where h_k are the terms comprising the electronic Hamiltonian, and n is the number of Trotter steps. Equation (1) becomes exact in the limit $n \rightarrow \infty$.

In our work, we empirically estimate the number of Trotter steps required to achieve convergence in the QPE algorithm, ensuring a sufficiently small error in the trotterized expansion. We plot the most likely estimated eigenvalue obtained using QPE for various combinations of ancilla qubits and Trotter steps for the (2/2) and (6/4) Hamiltonians, as shown in Fig. SI2 and Fig. SI3, respectively.

Fig. SI1 demonstrates that the choice of the number of Trotter steps, n , is a critical parameter for achieving high precision in the estimated phase. Examining the yellow circles, which represent the most-likely eigenvalues obtained with $n = 1$, it is clear that the results do not converge to the correct eigenvalue (indicated by the horizontal dashed line) or even reach chemical accuracy, as defined by the shaded gray area. For $n = 2$, represented by the green circles, the convergence improves significantly but still falls short of chemical accuracy. Even with 10 ancilla qubits – providing sufficient precision – the estimated eigenvalues remain outside the gray area.

Finally, for $n = 3$ and $n = 4$, the estimated eigenvalues show excellent agreement with the exact eigenvalue (except for results obtained with 10 and 12 ancilla qubits). This suggests that three Trotter steps are sufficient to achieve a reasonable approximation of the electronic Hamiltonian for this system.

A different scenario is observed in Fig. SI3, where the energy estimates are essentially independent of the number of Trotter steps. The yellow, green, and blue circles, corresponding to $n = 1$, $n = 2$, and $n = 3$ Trotter steps, respectively, overlap perfectly. As a result, the estimated results for $n = 2$ and $n = 3$ are shown only up to 10 ancilla.

In this case, achieving the required phase precision would necessitate 13 ancilla qubits. However, due to simulation limitations, this data point could not be obtained. Nonetheless, with 12 ancilla qubits, the estimated eigenvalues already fall very close to the shaded area.

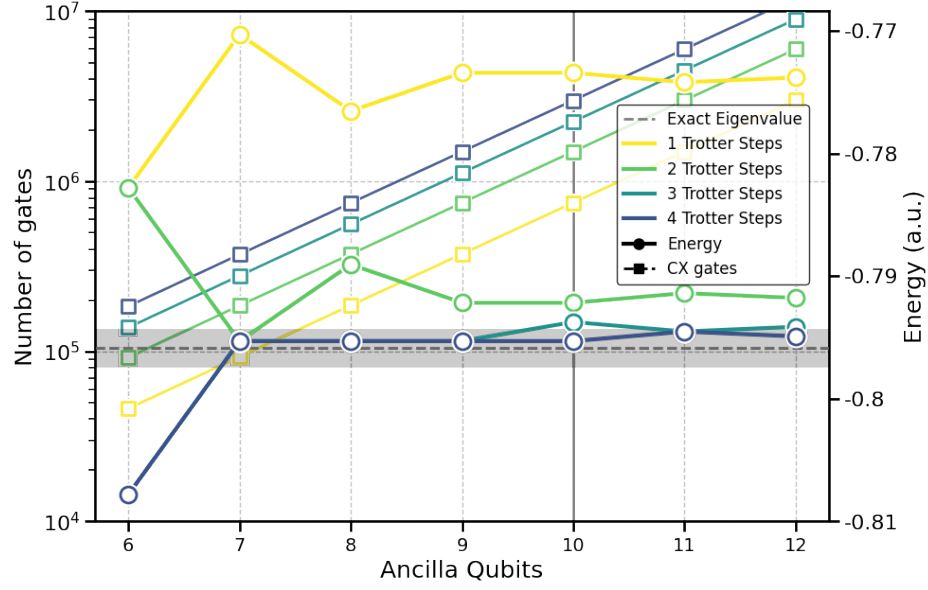


Fig. SI 2 Convergence results for the (2/2) Hamiltonian. The x-axis represents the number of ancilla qubits used to encode the binary representation of the phase. On the right y-axis, we plot the energy of the most-likely eigenvalue (empty circles), while the left y-axis shows the number of CNOT gates required for the calculation (empty squares). Lines connecting the circles and squares are included as visual guides. The results are computed using a varying number of Trotter steps, n , ranging from 1 (yellow) to 4 (purple). The exact eigenvalue, obtained by diagonalizing the Hamiltonian, is indicated by the horizontal dashed line. The gray-shaded area marks the chemical accuracy region, defined as $\lambda_{gs} \pm 1$ kcal/mol, where λ_{gs} represents the ground-state eigenvalue. Additionally, the horizontal gray line shows the number of ancilla qubits required to achieve a phase representation precision of at least chemical accuracy

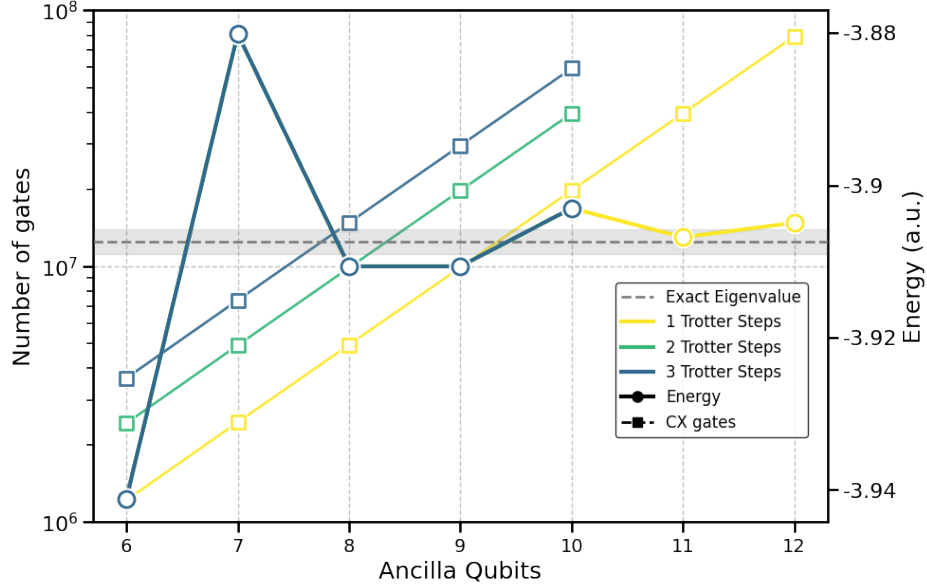


Fig. SI 3 Convergence results for the (6/4) Hamiltonian. The x-axis represents the number of ancilla qubits used to encode the binary representation of the phase. On the right y-axis, we plot the energy of the most-likely eigenvalue (empty circles), while the left y-axis shows the number of CNOT gates required for the calculation (empty squares). Lines connecting the circles and squares are included as visual guides. The results are computed using a varying number of Trotter steps, n , ranging from 1 (yellow) to 4 (purple). The exact eigenvalue, obtained by diagonalizing the Hamiltonian, is indicated by the horizontal dashed line. The gray-shaded area marks the chemical accuracy region, defined as $\lambda_{gs} \pm 1$ kcal/mol, where λ_{gs} represents the ground-state eigenvalue.

2 Variational Quantum Eigensolver

Variational Quantum Eigensolver results. For three small active spaces energy convergence of VQE was checked. The results for 10 runs mean and standard deviation are shown at Fig. SI4. For those experiments of VQE were run on ideal simulators, where the expectation values were computed from final state vector, not from sampled quasi-distribution. Optimizer iterations limit was set on 100 and error tolerance on 10^{-5} .

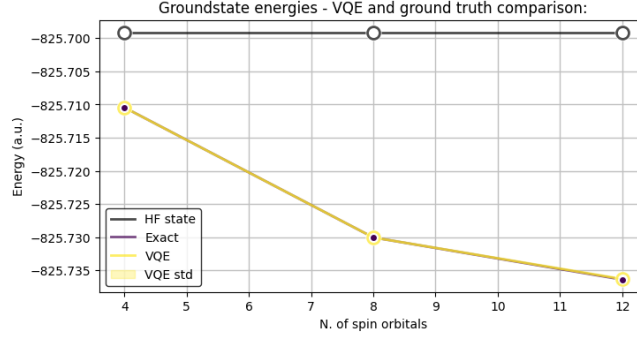


Fig. SI 4 Ground state energies obtained with VQE (mean and standard deviation from 10 trials) and explicit diagonalization of the Hamiltonian (“Exact” label). As a reference Hartree-Fock state energies was added (“HF” label). Experiments were run for three active spaces (2/2) - 4 qubits, (6/4) - 8 qubits and (10/6) - 12 qubits for iteration limit of 100, a optimizer error tolerance 10^{-5} .

Clifford states warm-start for the Variational Quantum Eigensolver. Warm start is a technique for variational optimization algorithms testing special set of initial parameters, allowing for faster convergence of the given problems. In VQE, UCCSD and other ansätze can be bind with special set of parameters, that yield circuit containing only Clifford quantum gates. [? ?]. That quantum circuit can be efficiently simulated on classical computers using so-called stabilizer simulators. [?] In this paper we have used this set of parameters to run initial few iterations of VQE on stabilizer simulators, to see if we can converge towards the energies lower than for HF state, which was initial starting point for default VQE implementation (that means that initially all parameters in UCCSD ansatz were zero). This approach, called CAFQA framework is described in this paper. [?] The results for active spaces (2/2) and (6/4) are shown in Fig. SI5. No improvement for two smallest active space sizes was observed over Hartree-Fock state initial set of parameters.

Adapth-VQE results for the Variational Quantum Eigensolver. Adapt-VQE is variation of VQE aiming to improve the convergence of VQE, by iteratively including more parameterized terms from ansatz, starting from a small number of terms. Per each sub-run, ansatz with first included terms is run on full VQE optimization, until it converge, and then another set of terms is included. For our case default VQE is

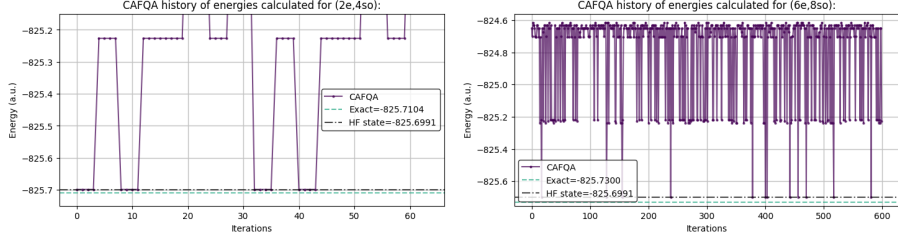


Fig. SI 5 CAFQA warm start energies history for two active space sizes (2/2) and (6/4).

systematically faster with smaller number of iterations per each run than Adapt-VQE (Fig. SI6).

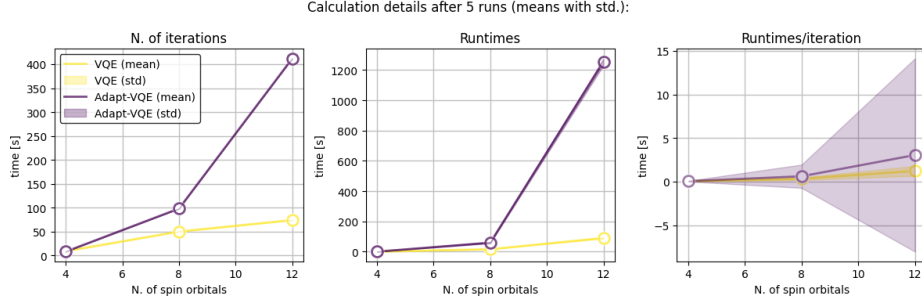


Fig. SI 6 VQE runs data for all Adapt-VQE and default VQE implementation in Qiskit for active space sizes from (2/2), (6/4) and (10/6).

Ansatz comparison for the Variational Quantum Eigensolver. For systematic comparison of the circuits yielded by different ansatz and their scaling towards the large active spaces, all shown at the Fig. SI7 types were synthesized with Qiskit and transpiled for simulator backends for Clifford+ R_z gates with all-to-all qubits connectivity.

UCCSD ansatz yield best circuit depth scaling and second best number of parameters scaling from the chemistry-informed ansatz, hence it was chosen for computations.

UCCSD ansatz terms contribution for the Variational Quantum Eigensolver. UCCSD ansatz, as any other ansatz, might contain the groups of gates, which are redundant to the convergence from HF state towards the true ground state configuration. If the ansatz might converge towards the ground state energy configuration with just minority of terms, there might be a potential for excluding some terms in the ansatz, hence reducing the circuit depth and its number of parameters. To check if this is the case for UCCSD in our problem, VQE was run iteratively for different number of groups of ansatz' terms sharing the same parameters, starting from single

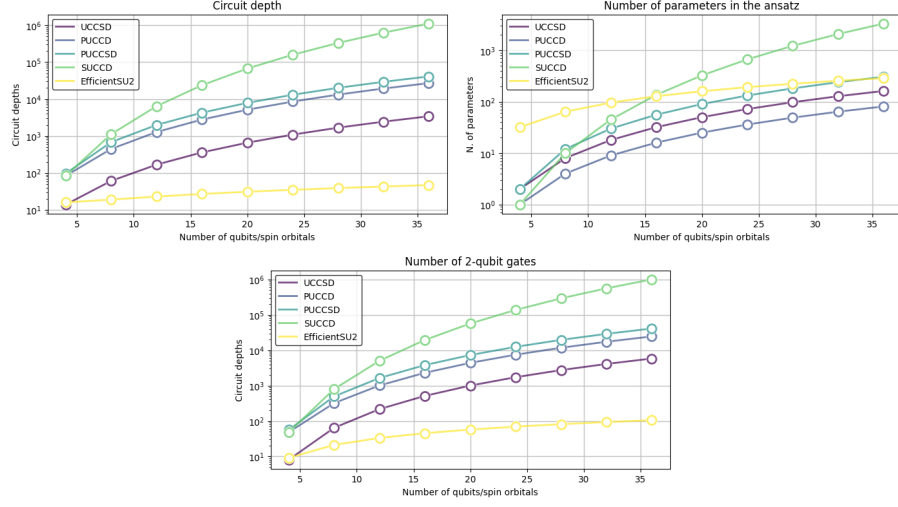


Fig. SI 7 Quantum circuit metrics for all available ansatzes in Qiskit synthesis for active space sizes from (2/2) to (34/18) with iterative increase of num. of electrons and num. of spin orbitals per 4.

group (so single parameters) and adding one group per each iteration until the VQE run for the whole ansatz. The energies obtained for those runs are shown at Fig. SI8. Each group of terms irregularly decrease the converged energy, but for two largest tested active spaces (after treating (2/2) as an outlier), most of the terms contribute to the energy convergence towards exact ground state energy and all the terms are needed to converge towards exact solution.

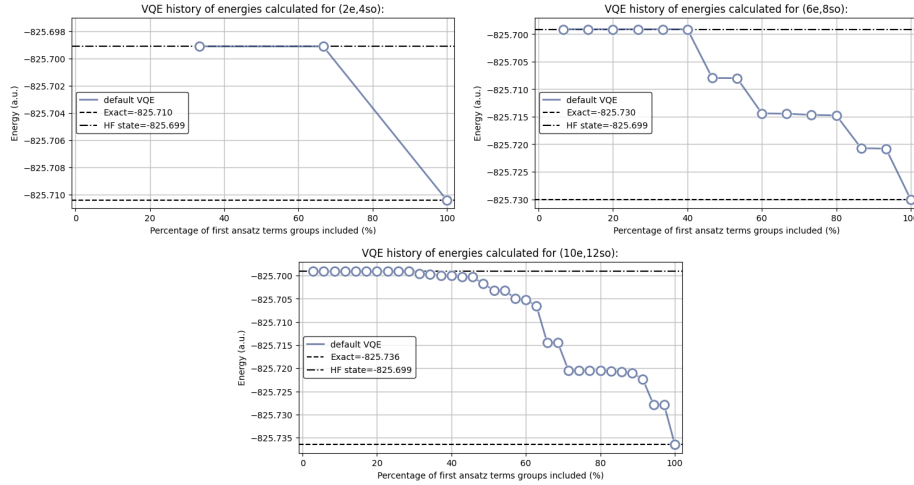


Fig. SI 8 Terms contribution to the exact ground start energy convergence history for three active space sizes (2/2), (6/4) and (10/6).

This show little room for improvement when it comes to excluding terms from the ansatz. Potentially, excluding first terms could be tested, if they contribute or not, but even if terms alone don't allow for the convergence towards lower energies, they may change the initial state, so that it becomes a proxy towards exact ground state converged with addition of latter terms.

3 Parameters for the Resource Estimation

For the quantum resource estimation, we utilized the resource estimation tool provided by Microsoft Azure. [?] The resource estimation for both VQE and QPE was conducted using the default parameters based on the physical qubit specification `qubit_gate_ns_e4`. These parameters correspond to future superconducting qubit architectures operating in the nanosecond regime. For this analysis, we stuck with all-to-all connectivity, since the real-backend connectivity overhead may be easily countered with more effective circuit synthesis [? ? ?], decomposition [? ?] and transpilation methods [? ? ?].

Specifically, gate and measurement operation times were assumed to be 50 ns and 100 ns, respectively. Idle, single-qubit, two-qubit, t-gate and measurement error rates were set to 10^{-4} , which represents an optimistic target for such quantum computing architectures.

4 DFT Calculations

Orbital	O2	Reactant	TS Diss	CIS	TS Diff	TRANS
2S	1.925	1.851	1.909	1.882	1.907; 1.871	1.858
2Pz	1.497	1.681	1.627	1.630	1.502 - 1.684	1.697
2Px	1.497	1.820	1.772	1.630	1.648; 1.658	1.678
2Py	1.060	1.079	1.297	1.730	1.754; 1.658	1.678
Total	5.979	6.431	6.606	6.891	6.811; 6.871	6.912

Table 1 Charge in each oxygen for a free O2 molecule (first column) and in the 5 geometries considered in NEB calculations. Only in the geometry corresponding to the TS diff configuration the charge is not the same in both atoms; both values are indicated in this case.

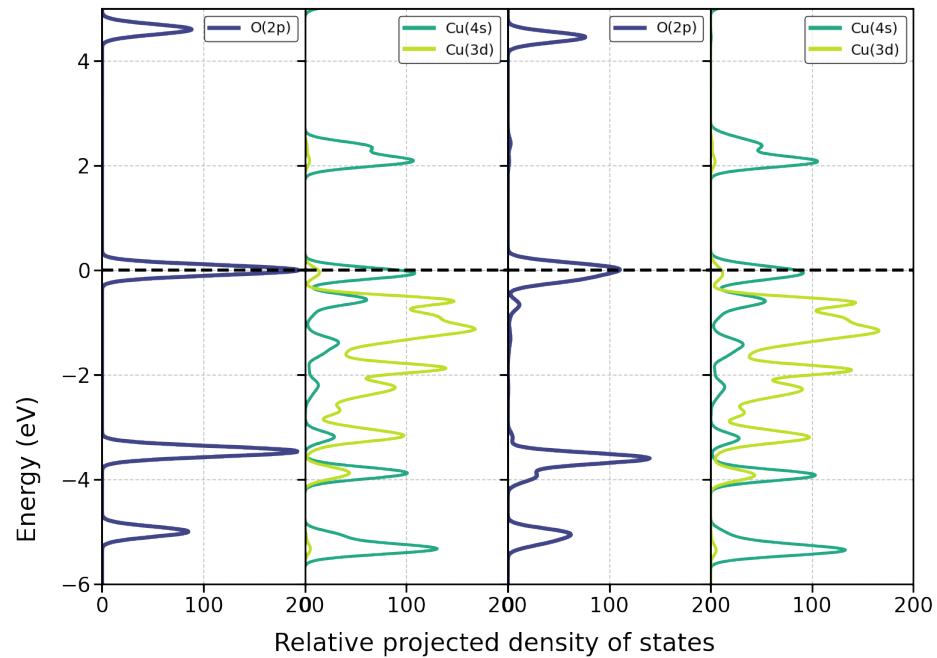


Fig. SI 9 Projected density of states (PDOS) for different atomic configurations: the first two panels represent the PDOS for a free O_2 molecule (O(2p) in blue) and a free Cu slab (Cu(4s) in green, Cu(3d) in yellow), while the last two panels correspond to a Cu slab system with an O_2 molecule placed far away. The energy (in eV) is shown on the vertical axis, and the relative projected density of states is plotted on the horizontal axis. The dashed line indicates the Fermi level.